Wind and Structures, Vol. XX, No. X (XXXX) 1–21
DOI: http://dx.doi.org/XXXXX

Topographic Effects on the Aerodynamic Design of the Julsundet Bridge

Giulia Pomaranzi*[1a], Filippo Calamelli[1b], Tommaso Argentini[1c], Alberto Zasso[1d] and Jungao Wang[2e]

[1]*Department of Mechanical Engineering, Politecnico di Milano, Via La Masa 1, 20156, Milan, Italy*
[2]*Norwegian Public Roads Administration, Stavanger, Norway*

(Received XXX, Revised XXX, Accepted XXX)

Abstract. The design of long-span bridges in complex terrains poses significant challenges, particularly in regions with pronounced topographic variations. This study examines the influence of topography on the wind characteristics and its implications for the aerodynamic design of the Julsundet Bridge, a planned long-span structure in Norway. Experimental data from terrain model wind tunnel tests are analyzed to assess how local topography affects wind speed, turbulence intensity, and directional changes along the bridge axis. Special focus is placed on the variations in angle of attack and velocity distribution induced by the surrounding fjords. Results showing terrain-induced effects on the wind directions, turbulence intensities and mean wind velocities are presented. The results highlight substantial spatial heterogeneity in wind characteristics, which must be considered in the prediction of the buffeting response of the bridge. These findings emphasize the importance of incorporating site-specific topographic effects in the design process to ensure optimal performance and safety of the bridge built in complex terrain.

Keywords: Wind tunnel tests; topographic effects; long-span bridges

1. Introduction

The aerodynamic design of long-span bridges is highly dependent on the turbulent characteristics of the wind. The aerodynamic behavior of these structures can vary significantly when transitioning from idealized smooth flow conditions to turbulent flows, highlighting the need for precise wind characterization during the design phase (Davenport and King

*Corresponding author, E-mail: giulia.pomaranzi@polimi.it
[a]Ph.D., E-mail: giulia.pomaranzi@polimi.it
[b]Ph.D., E-mail: filippo.calamelli@polimi.it
[c]Professor, E-mail: tommaso.argentini@polimi.it
[d]Professor, E-mail: alberto.zasso@polimi.it
[e]Ph.D., E-mail: jungao.wang@vegvesen.no

http://www.techno-press.org/?journal=sem&subpage=8 ISSN: XXXX-XXXX(Print), XXXX-XXXX(Online)

1990). Long-span bridge design typically relies on buffeting theory, as proposed by Davenport (1962), Scanlan (1978). Based on this theory, several numerical models have been developed in the past years to predict the aeroelastic response of bridges under turbulent winds. Nevertheless, due to the lack of reference results, validating these tools remains challenging (Diana et al. 2020a, b, 2022).

In this context, numerous full-scale measurement campaigns have been used to achieve this goal (as Cheynet et al. (2016), Fenerci et al. (2017)), with significant variability in observed responses. Such discrepancy seems to be related to the limitations in traditional approaches that assume a stationary and homogeneous wind field, treating turbulence characteristics as deterministic parameters, which may not accurately reflect real-world conditions (Fenerci and Øiseth 2017). Addressing these challenges requires a shift from traditional deterministic approaches to more refined statistical representations of wind fields. Such advancements aim to reflect the time-space variability of wind characteristics, reducing the uncertainties that contribute to response scatter (Calamelli et al. 2024). In this context, in-situ anemometric measurements, complemented by terrain model wind tunnel tests, play a crucial role (Lystad et al. 2018), allowing for the characterization of spatial and temporal variations in wind parameters, finally providing valuable input for more robust aerodynamic design frameworks.

The importance of accurately characterizing wind conditions becomes even more critical when bridges are situated in complex terrains. Recent studies in mountainous regions, such as those in southwest China (Zhang et al. 2022) and Norway (Fenerci et al. 2017, Castellon et al. 2022, Midjiyawa et al. 2021a, b), have utilized in-situ anemometric measurements to investigate local wind conditions. While these full-scale measurements provide valuable insights into the variability of local wind fields, their representativeness is limited to the specific mast locations. The challenge of transferring these measurements along the bridge span remains an open issue (Burlando et al. 2013, Midjiyawa et al. 2021a, Fenerci et al. 2023). To address this limitation, terrain model wind tunnel tests can be employed to study the spatial transfer of turbulence characteristics from mast locations to the bridge span. This methodology was applied by Lystad et al. (2018) at the Hardanger Bridge site, where anemometric measurements were complemented with terrain model wind tunnel tests to investigate spatial variations in wind field characteristics. Their findings emphasize that terrain model tests can provide reliable design specifications for wind characteristics, provided they are conducted at a sufficiently large scale to replicate extensive terrain features and consider a range of incoming wind directions.

Within this context, the proposed Ferjefri E39 project, led by the Norwegian Public Roads Administration (NPRA), presents all the challenges of realizing crossings between deep fjords and steep mountainous terrain. This ambitious project seeks to establish a continuous ferry-free highway along Norway's west coast, necessitating the construction of multi-kilometer fjord crossings, including the Julsundet Bridge. The steep topography of Norway's coastline is expected to induce significant wind modifications, highlighting the importance of detailed investigations into local wind conditions to ensure reliable predictions of buffeting loads.

As an initial step to document wind conditions at fjords, meteorological masts were installed on the shorelines of three different fjords to gather full-scale wind measurements.

These datasets serve as a foundation for calculating dynamic wind loads on long-span bridges. Studies by Midjiyawa et al. (2021a) and Midjiyawa et al. (2021b) analyze this multi-year data, focusing on integral flow and spectral characteristics to identify wind conditions relevant to bridge design. Among other challenges that come with full-scale measurements, they confirmed the difficulty of predicting the turbulence characteristics over the middle of the fjord based solely on the anemometer records. Moreover, for the Julsundet crossing, discrepancies in wind roses between the western and eastern shores emphasize the influence of local terrain. Variations in wind speed, turbulence intensity, and directional distribution further underscore the need for additional studies. Hence, to enhance the reliability of turbulent load predictions on fjord-crossing bridge decks, it is fundamental to complement anemometer measurements with terrain model wind tunnel tests or Computational Fluid Dynamics (CFD) simulations.

In this context, the present paper introduces the results of topography wind tunnel tests conducted at the Politecnico di Milano Wind Tunnel, commissioned by the Norwegian Public Roads Administration, to better understand the wind conditions relevant to the Julsundet Bridge design. The study focuses on terrain-induced modifications to wind characteristics at the Julsundet fjord site, emphasizing the spatial variability of mean wind speed, turbulence intensity, length scales, and wind angles critical for bridge design. Additionally, the results of this topographic study may be complemented by full-scale measurements from the aforementioned meteorological campaign, providing a basis for extending localized observations to characterize wind conditions along the bridge span.

2. Methodology

Wind tunnel tests were performed on a terrain model that replicates the most significant elevations surrounding the bridge. The resulting wind-field characterization at the bridge site wants to provide site-specific wind conditions to be considered in the bridge design process, especially for the estimation of the buffeting loads.

2.1 The Julsundet Bridge and its location

The bridge is located over the Julsundet fjord, as shown in Figure 1. It is oriented almost in a west-east direction, with the western side offset toward the south by approximately 13 degrees. The terrain on the western side of the bridge is mountainous, with peak elevations ranging from 600 to 700 meters and steep slopes. In contrast, the terrain on the eastern side is less steep but also features a mountain with a peak elevation of approximately 550 meters. The bridge has an open fetch over water of more than 5 km to both the south and north, perpendicular to its alignment.

The main span of the suspension bridge is 1625 m, with the road profile (top of the bridge deck at mid-span) located 76.52 m above mean water level.

2.2 Terrain model wind tunnel tests

To achieve an accurate representation of the wind field, a dedicated topographic study was performed in the boundary layer test section at Politecnico di Milano Wind Tunnel. A 10

(a) Location of the Julsundet Bridge (b) Fjord crossing

Fig. 1 Overview map showing location and orientation of the fjord crossing of interest for this study, the Julsundet Bridge. Image source: Google Earth, imagery date: 2024, accessed in January 2025.

km diameter surrounding area was reproduced in the boundary layer test section, assuming a length scale of 1:1000 (Fig. 2). This scale allowed for an accurate representation of the terrain elevations closest to the Julsund Bridge site, which are expected to have the greatest impact on the local wind flow conditions.

Due to the presence of relatively tall mountains near the site, truncation of the terrain model was necessary when modeling a 10 km diameter area. Such abrupt changes can noticeably affect flow characteristics (Peng et al. 2018, Yu et al. 2024). To mitigate these effects and ensure accurate predictions of wind conditions at the bridge location, a Boundary Transition Section (BTS) was implemented. A series of preliminary steady-state CFD simulations were conducted to validate the BTS's effectiveness and confirm that truncation did not introduce distortions. These simulations focused on extracting mean wind profiles at the bridge location for various wind directions, using a larger domain of approximately $400\,\mathrm{km}^2$ surrounding the bridge. The results obtained from this large domain were then compared to those from a smaller domain, roughly 10km in diameter — corresponding to the area intended for physical reproduction in the wind tunnel. In the smaller domain, a slipway was added at the truncation boundaries to smooth the transition. The finalized BTS geometry is shown in Fig. 3, with the transition regions highlighted in yellow. This comparison confirmed that the truncation did not significantly alter the wind profiles, thus validating the reliability of the BTS.

According to wind roses derived from full-scale measurements at the bridge site Midjiyawa et al. (2021a), the strongest winds in the Julsundet area predominantly originate from the west-northwest, while weaker wind events are observed from the south. These observations guided the selection of wind directions used in the terrain model wind tunnel tests, which also included directions aligned with the longitudinal axis of the bridge—primarily relevant for the tower design. In total, 16 different incoming wind directions were tested. These included directions perpendicular and parallel to the bridge axis, as well as yawed angles of 10°, 20°, 30°, and 45° relative to the normal axis, covering the northwest, southwest, and southeast sectors, as illustrated in Fig. 4.

Under each wind direction, the mean wind speed, mean wind direction, turbulence in-

Fig. 2 The terrain model in the wind tunnel test section

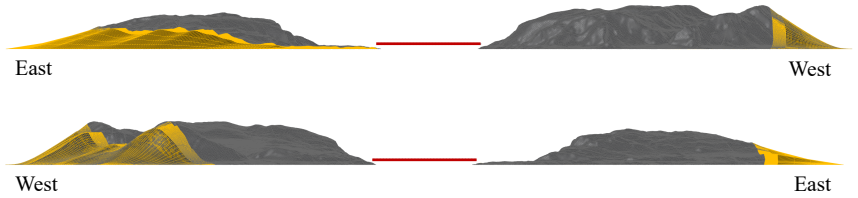

Fig. 3 The BTS model: view from North (top) and South (bottom). Yellow areas represent the transaction sections while the red line clarifies the bridge location

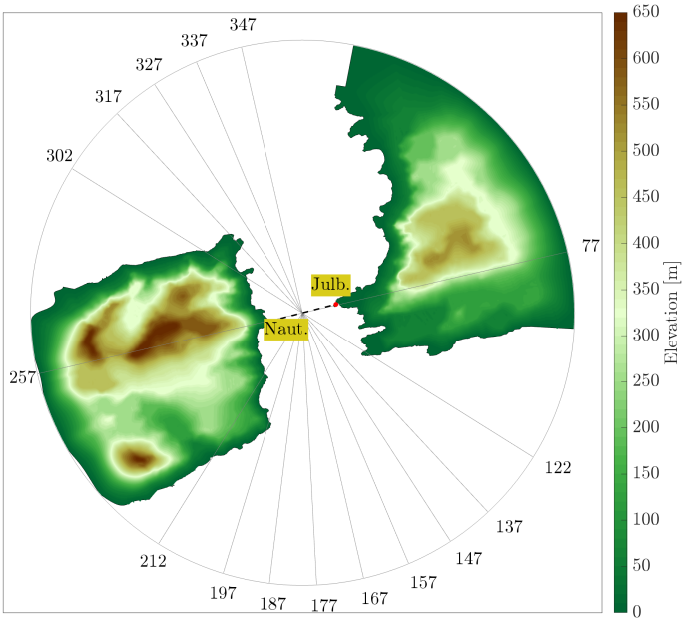

Fig. 4 Sketch of the BTS model with the considered inlet wind directions.

tensity and wind spectrum were measured at 50 m resolution along the bridge deck and two bridge towers. The wind coherences were also established using 3 separation lengths, i.e. 25, 50, and 75 m distance along the bridge axis. All the velocity measurements were carried out by means of 4 multi-hole pressure probes able to resolve 3-components of velocity in real-time (Cobra Probes, TFI (2008)), acquired simultaneously with 2000 Hz sampling frequency. Assuming a full-scale wind speed of 38.56 m/s at deck level (10-minute mean wind speed with a 50-year return period) and a reference wind speed of 9 m/s in the wind tunnel, the velocity scale is $\lambda_U = 1/4.3$. Given a length scale of $\lambda_L = 1/1000$, the time scale can be computed as $\lambda_T = \lambda_L/\lambda_U \approx 1/233$. The acquisition time is set to 60 s in model scale, corresponding to approximately 233 minutes in full scale, allowing for the estimation of statistically meaningful quantities.

The inlet wind profiles for the topographic tests were derived from full-scale measurements conducted between 2014 and 2019 using two 50 m high masts located at the positions of the bridge towers (Julbo and Nautneset). The target profiles were computed by estimating the roughness length, z_0, from the measured along-wind turbulence intensity, under the assumption that turbulence intensity is inversely proportional to $\ln\left(\frac{z}{z_0}\right)$.

To establish a consistent inlet configuration for the wind tunnel tests, target profiles for various wind directions were grouped according to the corresponding exposures. Figure 5 illustrates the comparison between the target profiles and those achieved in the wind tunnel. The first two subplots represent northern exposures (for inlet winds from 257° to 347° and 77°), while the last two correspond to southern exposures (from 122° to 212°). Overall, a good agreement was observed for the mean velocity profiles.

The wind tunnel inlet profiles were documented using four Cobra Probes spaced 0.25 m apart in the lateral cross-wind direction, enabling the computation of longitudinal (along-wind) and lateral integral length scales. At deck level, relying on the autocorrelation function, the integral length scales were estimated as $L_u^x \approx 850$ m and 700 m (full scale) for northern and sourthern wind tunnel realizations respectively. These values are significantly larger than the expected full-scale length of 162 m at deck height, as prescribed by the N400 standard. This discrepancy indicates that wind tunnel inlet flow is characterized by a greater spatial correlation than the expected full-scale counterpart.

To address the mismatch in length scale, all results presented hereafter are normalized with respect to the inlet conditions. This approach ensures that the terrain-induced modifications to the flow are appropriately captured and highlighted, regardless of the discrepancies in spatial correlation between the wind tunnel and full-scale conditions.

3. Results - Terrain Model Wind Tunnel Tests

This section presents the results of the terrain model tests. The initial analysis characterizes the wind field as a function of the incoming wind direction, with velocity components expressed in a wind-axis coordinate system. Subsequently, to facilitate interpretation in the context of bridge design, the results are re-expressed in a reference system aligned with the deck axis. This transformation enables the definition of key design-relevant quantities, such as the wind velocity component normal to the deck axis and the angle of attack.

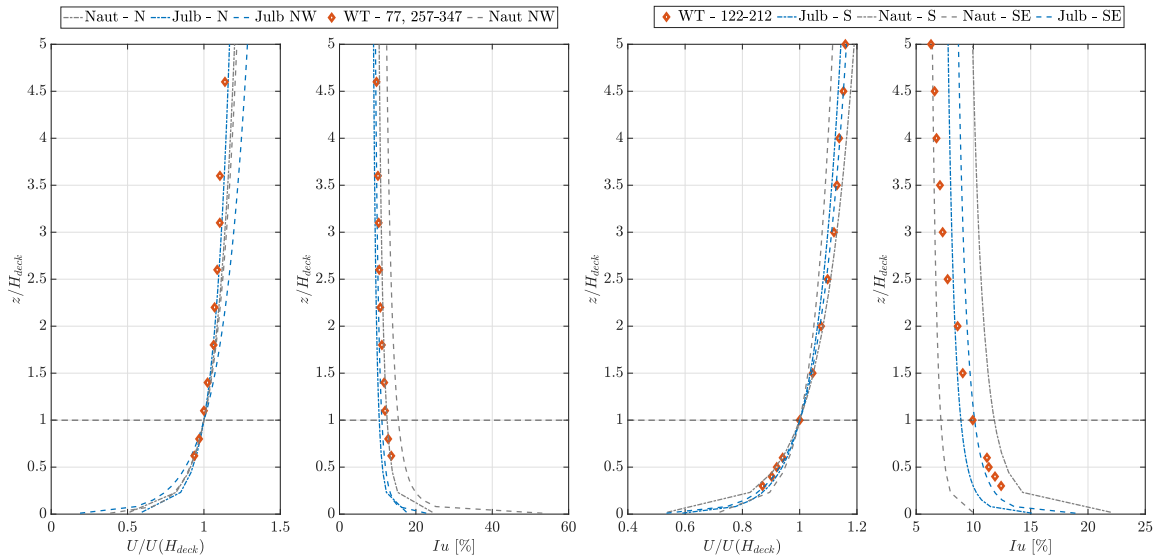

Fig. 5 Inlet profiles for the terrain wind tunnel tests. The first and second subfigures show the profiles for northern inlet directions, presenting mean wind speed and turbulence intensities. The third and fourth subfigures correspond to southern inlet directions.

All results are presented in a non-dimensional form. Velocity measurements are normalized by the reference wind speed U_{ref}, defined as the mean wind speed at deck height in the inlet profile, measured at the beginning of the turntable and at the center of the test section. Similarly, turbulence intensity profiles are normalized with respect to the corresponding turbulence intensity in the inlet profile at deck height, $I_{u,ref}$.

3.1 Wind characterization - Wind axis

3.1.1 Conventions

Two reference systems are defined in this study, both following wind-axis conventions:

- Inlet-aligned reference system - x_0, y_0, z_0: this reference system is defined with respect to the inlet wind conditions in the wind tunnel (Fig. 6a). Its x-axis points in the direction of the incoming wind speed at the tunnel inlet, the y-axis is perpendicular to the x-axis and points to the left when looking downstream, and the z-axis is perpendicular to the xy-plane, oriented according to the right-hand rule. This system is used to describe the undisturbed incoming flow prior to its interaction with the terrain model.
- Wind-aligned reference system - x, y, z: this reference system is defined with respect to the local mean wind velocity vector measured at each location along the bridge axis during the terrain model wind tunnel tests (Fig. 6c). Its x-axis aligns with the direction of the measured mean wind velocity $\bar{U}$, the y-axis is perpendicular to the x-axis and points to the left when looking downstream along the local wind direction, and the z-axis completes the right-handed system.

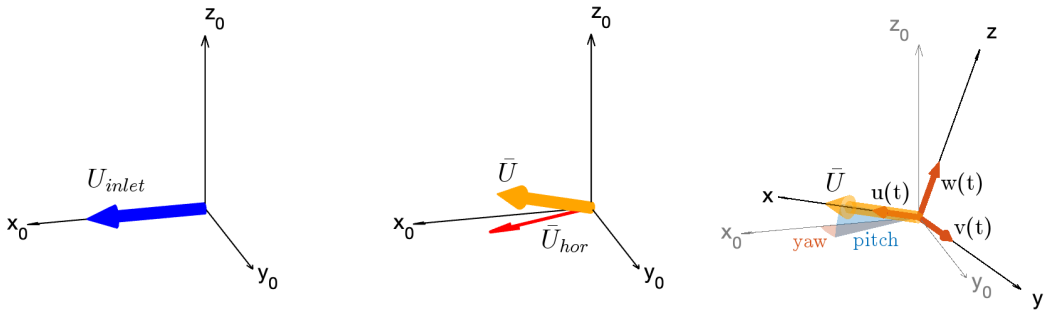

(a) (b) (c)

Fig. 6 Reference systems: inlet-aligned reference systems (a,b) and wind-aligned reference system (c).

To fully describe the orientation of the velocity vector, yaw and pitch angles are introduced. These angles are defined in the inlet-aligned reference system as follows:

- Yaw angle: defined in the horizontal plane (x_0, y_0), it is the angle between the x_0 axis and the projection of the mean velocity vector onto the horizontal plane $\bar{U}_{hor}$. Positive yaw corresponds to a counterclockwise rotation when viewed from above.
- Pitch angle: defined in the vertical plane, it is the angle between the mean velocity vector $\bar{\mathrm{U}}$ and its projection onto the horizontal plane (x_0, y_0). Positive pitch corresponds to an upward-directed velocity vector.

Finally, Section 3.2 presents wind measurements projected into a bridge-aligned reference system, as this is the typical way of expressing wind features for bridge design purposes.

3.1.2 Mean Wind Speed and Turbulence Intensities

Figure 7 illustrates the normalized mean wind speed and along-wind turbulence intensity profiles measured along the bridge axis for various inlet wind directions. For an easterly wind (77°, aligned with the deck axis), the interaction with the eastern fjord leads to a reduction in mean wind speed, resulting in uniform wind conditions along the span. This uniformity is accompanied by a significant increase in turbulence intensity, exceeding twice the reference value, $I_{u,\mathrm{ref}}$. Conversely, westerly winds (257°) exhibit a strong gradient along the bridge axis due to the interaction with peaks near the western fjord. The mean wind speed increases from west to east, with a westward sheltering effect causing localized reductions in wind speed up to $0.5U_{\mathrm{ref}}$. Turbulence levels show an inverse trend, peaking near Nautneset before gradually decreasing toward Julbo.

For south-easterly winds (122°), the wind properties along the deck remain relatively uniform, with mean wind speeds slightly below U_{ref}. When the inlet direction shifts to 137°–177°, channeling effects result in accelerated flow, causing mean wind speeds to exceed U_{ref}, while turbulence levels are reduced compared to inlet conditions.

Winds from the south (187° and 197°) display a significant reduction in mean wind speed due to interactions with the western fjord. The reduction extends up to one-fourth and

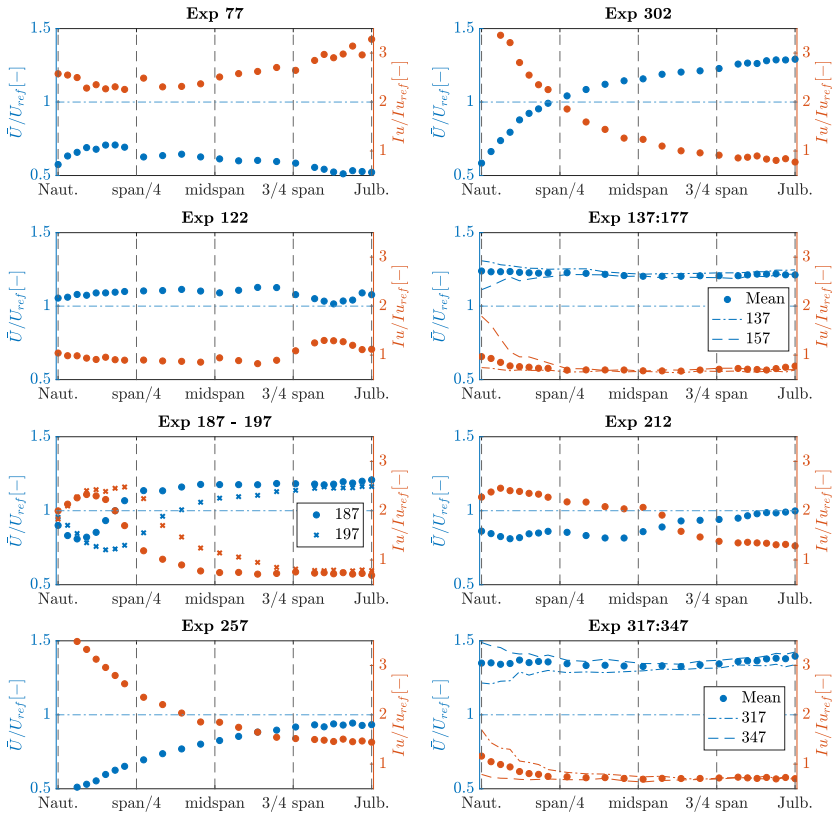

Fig. 7 Mean wind speed (normalized with respect to the reference wind speed) and along-wind turbulence intensity measured along the bridge longitudinal axis for each exposure angle.

midspan for 187° and 197°, respectively. Turbulence intensity increases correspondingly, peaking at locations where the mean wind speed is lowest. At 212°, the profiles become more uniform as the bridge axis lies entirely within the wake of the western fjord.

For northern wind directions, significant variations are observed. At 302°, interaction with the western fjord leads to an increase in mean wind speed from Nautneset to Julbo, with a doubling of speed along the span. Turbulence intensity at Nautneset exceeds three times $I_{u,\mathrm{ref}}$ but reduces to $I_{u,\mathrm{ref}}$ near Julbo. Winds from 317°–347° result in nearly uniform profiles along the span, with mean wind speeds exceeding the inlet due to channeling effects and turbulence intensities comparable to inlet conditions.

3.1.3 Pitch and Yaw angles

The pitch and yaw angles along the bridge axis are shown in Fig. 8. A yaw angle of zero corresponds to flow aligned with the inlet wind direction, while a positive pitch angle indicates an upward vertical component. For easterly and southerly winds (77°–177°), pitch

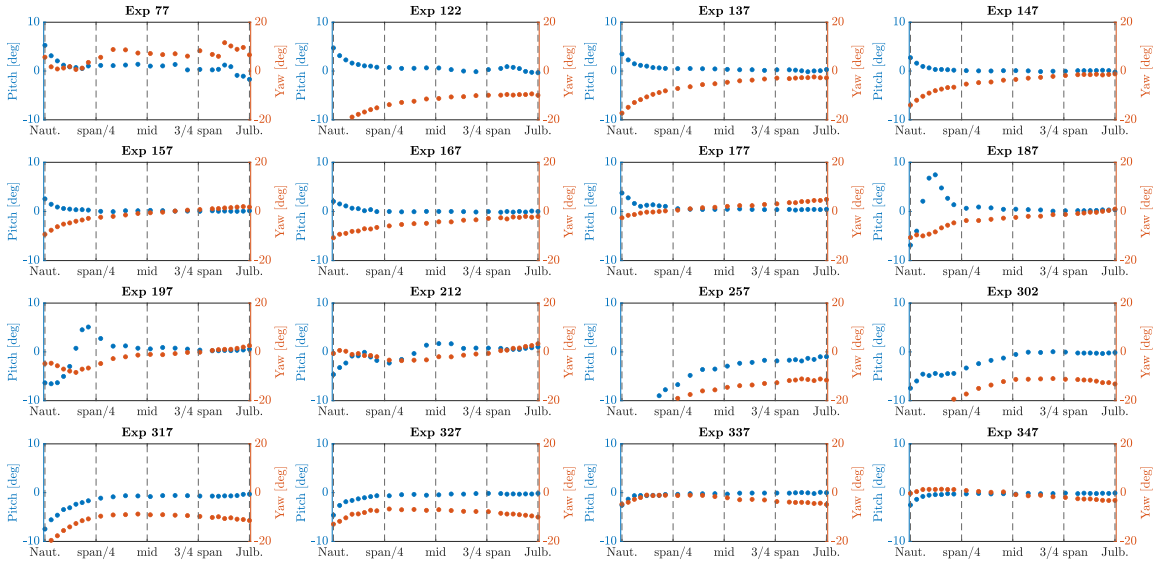

Fig. 8 Pitch and yaw angles variation along the longitudinal bridge axis, for each exposure angle

angles at Nautneset are consistently positive due to flow ascent over the fjord. The angles decrease along the bridge axis, reflecting the diminishing vertical component of the flow near Julbo. The yaw angles exhibit an easterly deflection, peaking at approximately 20° near Nautneset for inlet winds at 137° and 147°, before aligning with the inlet direction toward Julbo.

For south-southwest winds (187°, 197°, and 212°), downwash effects near Nautneset result in negative pitch angles, particularly for 257°, where the inlet wind aligns with the bridge axis. Westerly and northwesterly winds (257°–347°) exhibit similar trends, with negative pitch angles caused by downwash as the flow overtakes the western fjords. The most significant downwash occurs for westerly winds. Northerly winds (302°, 317°, and 327°) show negative yaw angles ranging from -20° to -10°, indicating alignment with the open fetch. For nearly orthogonal winds, yaw angles are negligible, with pitch angles remaining near zero except at Nautneset.

3.1.4 Longitudinal length scales

The longitudinal integral length scale, L_u^x, was estimated using the auto-correlation function derived from the Cobra Probe measurements to quantify the size of turbulent structures. Results for various wind directions are presented in Figure 9, normalised by the corresponding inlet values.

For inlet wind directions aligned with the bridge axis (77° and 257°), L_u^x and L_v^x are significantly smaller than their respective inlet values, indicating the presence of smaller turbulent structures generated by the interaction of the flow with the surrounding fjords.

For southern exposures (122° to 177°), the integral scales of the u and v components are approximately equal to the inlet values. In contrast, L_w^x generally exceeds the inlet values,

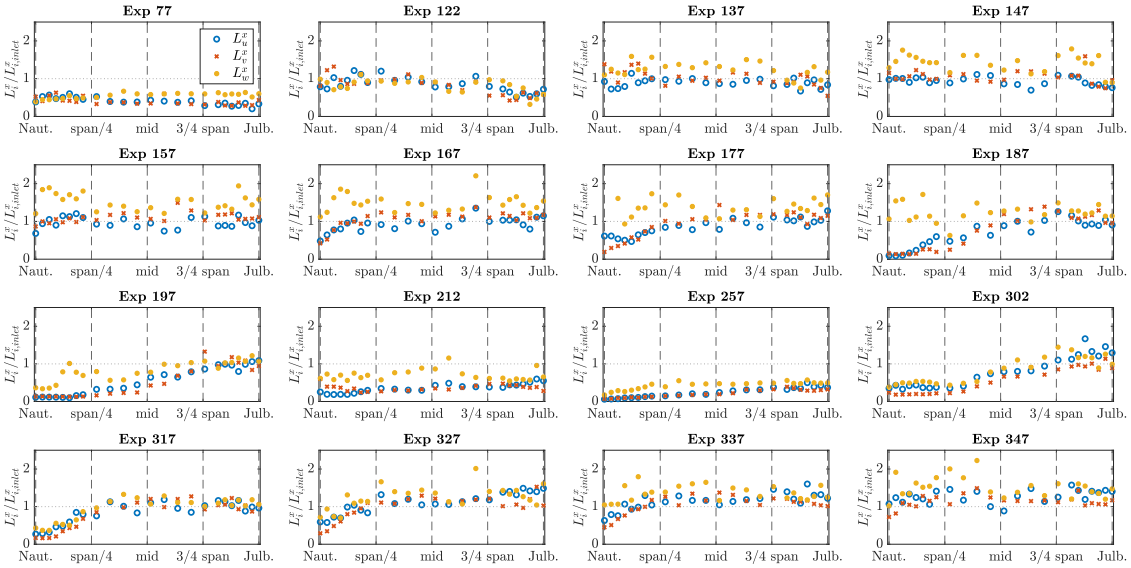

Fig. 9 Integral length scales L_u^x, L_v^x, and L_w^x normalised to the inlet values at deck level.

suggesting increased vertical correlation under these conditions.

When the inlet wind shifts to the 187°–212° range, interaction with the southern part of the western fjord results in $L_u^x/L_{u,\text{inlet}}^x$ values smaller than unity over the first half of the span, again indicating smaller turbulent vortices.

For winds approaching from the north, nearly orthogonal to the deck axis (327° and 347°), the integral scales for the u and v components remain consistent with inlet conditions, while L_w^x increases, reflecting enhanced vertical correlation. For wind exposures at 302° and 317°, a progressive increase in longitudinal integral length scales is observed from Nautneset to Julbo, attributed to the interaction of the flow with the western fjord.

To understand why L_w^x generally exceeds the inlet values - especially for those exposures almost normal to the bridge axis, the spectra of the measured vertical velocity component w were compared with the inlet spectrum. The integral length scale L_w^x is related to $S_w(f)$ through:

$$L_w^x \propto \frac{U}{\sigma_w^2} \int_0^\infty \frac{S_w(f)}{f}\, df, \tag{1}$$

where U is the mean wind speed at the considered height, $S_w(f)$ is the power spectral density of the vertical velocity fluctuations, and σ_w^2 is their variance.

This relation shows that L_w^x is influenced by the spectral energy weighted by $1/f$, such that low-frequency components contribute more strongly to its value. In other words, fluctuations occurring over longer timescales (lower frequencies) correspond to larger coherent structures in space, dominating the integral length scale calculation. Therefore, increased energy at low frequencies results in higher L_w^x values.

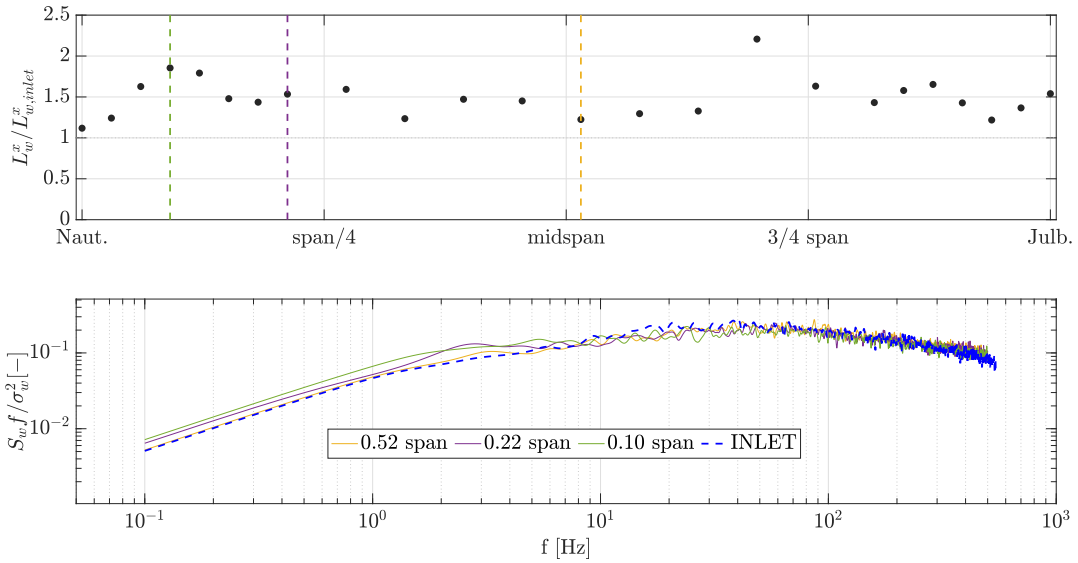

Fig. 10 Top: Ratio of the integral length scale of vertical velocity fluctuations, L_w^x, to the inlet value, $L_{w,\text{inlet}}^x$, at different positions along the bridge span. Bottom: Non-dimensional power spectral density of vertical velocity fluctuations w measured at several locations (0.10, 0.22, and 0.52 of the bridge span) compared with the inlet spectrum.

The upper plot of Figure 10 shows $L_w^x/L_{w,\text{inlet}}^x$ for an inlet wind direction of 167°. The lower plot reports the non-dimensional power spectral densities (PSDs) of w at various locations (0.10, 0.22, and 0.52 along the bridge span) alongside the inlet PSD. It can be observed that, in the lower frequency range, the energy content measured during the terrain model tests exceeds that of the inlet, consistent with the integral length scale ratio being greater than unity.

3.1.5 Wind Spectra

For the deck measurements, single-point spectra $S_u(f)$ were computed for each configuration to assess the variations in spectral behaviour. As an example, Fig. 11 illustrates the wind spectra of the along-wind component for the 302° exposure, moving from Nautneset toward the midspan of the bridge. The spectra are normalised with respect to f/σ_u^2, where f is the frequency and σ_u^2 is the variance of the along-wind component u. For reference, the von Kármán spectrum is also shown. At locations closest to Nautneset, the high-frequency content of the spectra exhibits deviations from the slope predicted by the Von Karman spectrum, attributed to the elevated turbulence intensities recorded at these positions. This behaviour reflects the influence of the surrounding terrain near the fjord, which generates highly turbulent flow with small-scale vortices. However, as the measurement locations progress toward the midspan of the bridge, the spectral behaviour increasingly aligns with the inlet conditions. This indicates a diminishing impact of the terrain, with the wind field becoming more representative of the inlet flow.

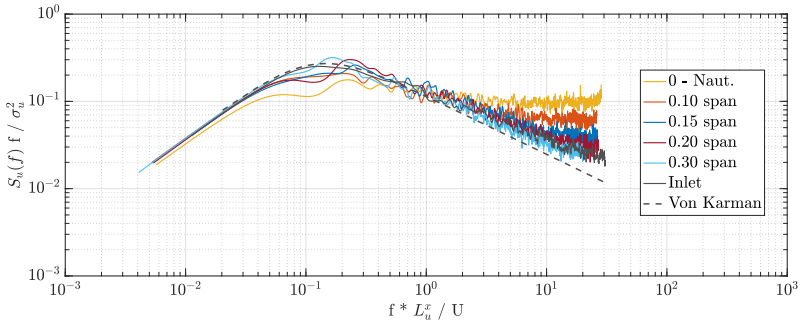

Fig. 11 Single-point wind spectra estimated for different locations along the deck axis, spanning from Nautneset to the 1/3 of the span for inlet wind from 302°.

3.1.6 Co-coherence function coefficients

To further characterize the spatial correlation of turbulent velocity fluctuations, measurements from the four Cobra probes along the deck axis were used to estimate the coherence function. Specifically, the real part of the normalized cross-spectrum provides information about the spatial correlation (Ropelewski, Tennekes, and Panofsky 1973):

$$\mathrm{Coh}_{i,\mathrm{hor}} = \frac{\mathrm{Re}\left(S_i(\zeta_1,\zeta_2,f)\right)}{\sqrt{S_i(\zeta_1)S_i(\zeta_2)}}, \quad i = u,v,w \tag{2}$$

where $S_i(\zeta_1)$ and $S_i(\zeta_2)$ are the one-point spectra estimated at locations ζ_1 and ζ_2 respectively and $S_i(\zeta_1,\zeta_2,f)$ is the two-point cross-spectral density estimate between these locations. Coherence functions are here defined considering the velocity components in a wind-aligned reference system.

During the experiments, the Cobra probes were positioned along the bridge axis. Considering the flow is not always orthogonal to the deck axis, the separation between a pair of probes includes both along-wind (dx) and lateral (dy) components. Therefore, instead of the Davenport model (Davenport 1961) commonly used in wind engineering, a modified coherence model for horizontal separation was adopted, incorporating both separation lengths dx and dy, alongside a cosine term to account for possible negative coherence (time-lag effects), as proposed by Peng et al. (2018). This modification provides a more accurate characterization of wind coherence based on the experimental data. The coherence function is expressed as:

$$\mathrm{Coh}_{i,\mathrm{hor}} = \exp\left(-\frac{f}{0.5\big(U(\zeta_1)+U(\zeta_2)\big)}\sqrt{(C_{ix}\,dx)^2+(C_{iy}\,dy)^2}\right)\cdot \cos\left(\frac{2\pi f\,dx}{0.5\big(U(\zeta_1)+U(\zeta_2)\big)}\right), \quad i = u,v,w \tag{3}$$

where $U(\zeta_1)$ and $U(\zeta_2)$ are the mean wind speed at two different locations, dx and dy are the separation lengths of the two wind components along the longitudinal and lateral

directions, f is the frequency in Hz, C_{ix} and C_{iy} are the coherence coefficients for the $i-th$ wind component separation. It can be observed that there would be infinite pairs of C_{ix} and C_{iy} that would give equally good fitting, since it is the term $\sqrt{(C_{ix}\,dx)^2+(C_{iy}\,dy)^2}$ that governs the decay curve of the coherence. Therefore, the following relationship between C_{ix} and C_{iy} based on both measurements (using limited number of pure longitudinal dx and lateral dy separations) and literature (Solari and Piccardo 2001) is adopted:

$$\begin{bmatrix} C_{ux} \\ C_{vx} \\ C_{wx} \end{bmatrix} = \begin{bmatrix} \frac{1}{3} C_{uy} \\ \frac{1}{4} C_{vy} \\ \frac{1}{6} C_{wy} \end{bmatrix} \tag{4}$$

Assuming as independent coordinate $f^* = f\,dy/\left[0.5\big(U(\zeta_1)+U(\zeta_2)\big)\right]$ and considering the relationships from Eq. 4, Equation 3 can be rewritten as:

$$\mathrm{Coh}_{u,\mathrm{hor}} = \exp\left(-f^* C_{uy}\sqrt{\frac{1}{9}\left(\frac{dx}{dy}\right)^2+1}\right)\cdot\cos\left(2\pi f^*\frac{dx}{dy}\right) \tag{5}$$

$$\mathrm{Coh}_{v,\mathrm{hor}} = \exp\left(-f^* C_{vy}\sqrt{\frac{1}{16}\left(\frac{dx}{dy}\right)^2+1}\right)\cdot\cos\left(2\pi f^*\frac{dx}{dy}\right) \tag{6}$$

$$\mathrm{Coh}_{w,\mathrm{hor}} = \exp\left(-f^* C_{wy}\sqrt{\frac{1}{36}\left(\frac{dx}{dy}\right)^2+1}\right)\cdot\cos\left(2\pi f^*\frac{dx}{dy}\right) \tag{7}$$

As an example, Fig. 12 illustrates the coherence estimation for the along-wind u, cross-wind v, and vertical components w, compared with the fitted model described by Eq. 3. The results correspond to the inlet wind at 212°, evaluated at 3/4 of the span on the eastern side. The proposed model is able to accurately estimate coherence in the low-frequency range while also capturing the negative coherence observed at higher frequencies.

According to the coherence model considered here, the decay of the coherence function is dictated by both the exponential and cosine terms. Consequently, the coefficients C_{iy} alone are not fully representative of the coherence function's evolution. The influence of the cosine term could become particularly significant when the longitudinal spacing dx between the Cobras is comparable to the spanwise spacing dy. Moreover, since the cosine term depends on dx, its value varies with exposure, as dx changes depending on the yaw angle. For this reason, the coefficients C_{iy} presented in the following are normalized with respect to their value at midspan for each exposure. This normalization choice accounts for differences across exposures and enables a more consistent comparison along the bridge axis, where similar dx values are found for each exposure.

Coefficients related to the u, v, and w components showed similar trends; thus, the description in the following is limited to the vertical component. However, analogous considerations apply to the alongwind and lateral components. The resulting trends for the $C_{w,y}$ coefficient along the deck axis are presented in Fig. 13, with the left and right subplots corresponding to southern and northern exposures, respectively.

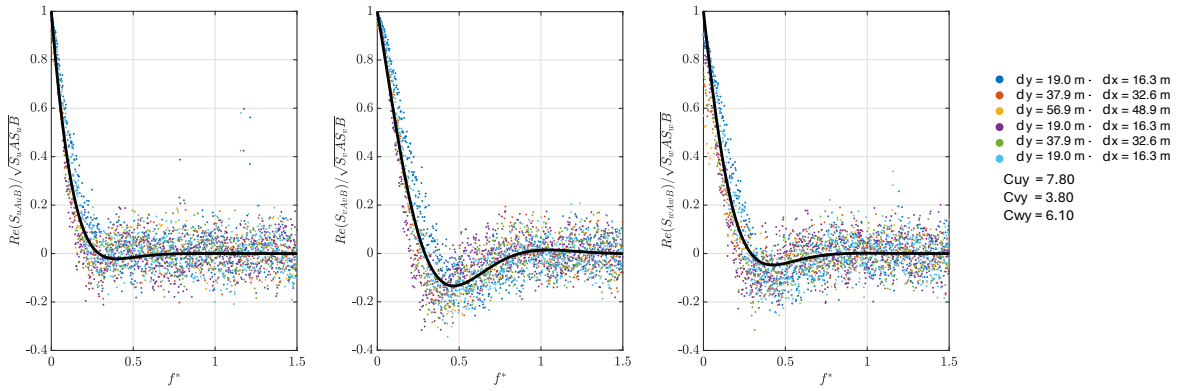

(a) u component (b) v component (c) w component

Fig. 12 Example of the estimated wind coherence for the along-wind (a), cross-wind (b), and vertical co-coherence (c) components, compared to the fitted model from Eq. 3.

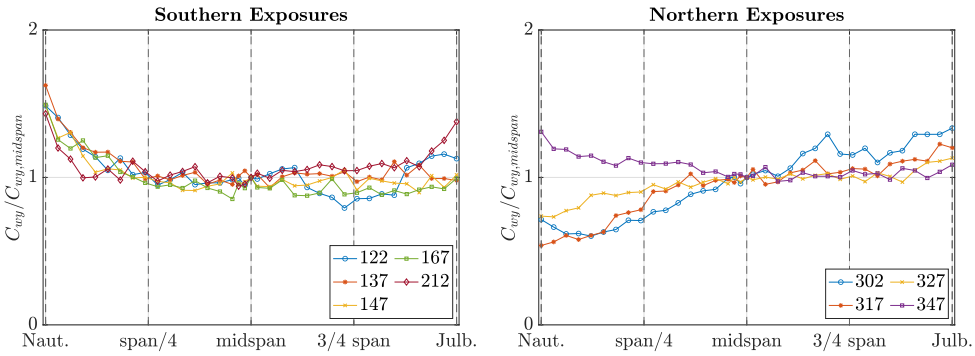

Fig. 13 Trend of the estimated $C_{w,y}$ coefficient along the bridge longitudinal axis. Left plot refers to inlet direction from South and right plots shows the northern inlet winds.

For southern exposures, the $C_{w,y}$ coefficient exhibits a consistent trend, with the highest values at Nautneset and a decreasing pattern toward Julbo. Since $C_{w,y}$ represents the decay coefficient of the coherence function, this indicates increasing coherence of the vertical velocity component (w) when moving from Nautneset to Julbo, likely due to the interaction with the prominent elevation at Nautneset.

In contrast, northern exposures display an increasing trend in $C_{w,y}$ from Nautneset to Julbo. Stronger gradients along the bridge axis are observed for inlet wind directions more influenced by the western fjord. It appears that the downward-deflected flow, due to the interaction with the fjord, for exposures 302° and 317°, exhibits higher correlation in the vertical component relative to midspan.

3.2 Wind Characterization - Bridge Axis

For bridge design purposes, wind features are typically expressed in a reference system aligned with the deck axis. The results presented earlier are projected onto this bridge-aligned reference system, focusing on the normal component of the velocity vector relative to the deck axis and the angles that define the orientation of the velocity vector. These angles include the angle of attack (AoA), representing the orientation of the velocity vector in a plane normal to the deck axis. A positive angle of attack indicates a positive vertical component of the wind velocity vector.

Fig. 14 presents the normal component of the velocity vector's horizontal plane projection relative to the bridge axis (U_n, left subplot) and the angle of attack (right subplot) for all inlet directions from the North. For wind from 302°, the sheltering effects of the western fjord lead to a significant reduction in U_n at Nautneset, where it drops to half the incoming wind speed. Moving toward Julbo, the wind speed normal to the bridge axis recovers. The angle of attack is negative (downward-directed flow) at Nautneset, influenced by downwash effects as the flow passes over the fjord. This results in an AoA smaller than $-5°$, potentially impacting the aerodynamic stability of the deck, though at lower wind speeds. Negative AoA values characterize the left half-span of the bridge, transitioning to near-zero AoA closer to Julbo. For inlet wind directions between 317° and 347° (grouped due to shared characteristics), the channelling effect previously highlighted is translated into U_n exceeding the reference wind speed by 20%, while the AoA starts at approximately $-5°$ at Nautneset (due to local orography) and quickly stabilizes to near-zero for three-quarters of the span.

Fig. 15 illustrates the velocity component normal to the bridge axis and the angle of attack for inlet directions ranging from 122° to 212°. For wind from 122°, orographic effects cause a gradual reduction in U_n/U_{ref} from unity at Nautneset to 0.8 at Julbo. The AoA is nearly zero at Julbo and the midspan but increases to 5° near Nautneset, reflecting the flow's tendency to rise over the western fjord. For wind directions between 137° and 177°, orographic effects are minimal. Here, U_n remains nearly constant and exceeds the reference wind speed due to the previously noted channeling effect. The AoA is close to zero for most of the span, except near Nautneset, where it remains slightly positive ($\approx 3°$). For wind from 187° or 197°, interactions with the western fjord cause U_n/U_{ref} to fall below unity at Nautneset but recover to unity toward Julbo. The AoA transitions from negative to positive values, indicative of a "twist" along the bridge axis, stabilizing near zero from midspan to Julbo. Finally, for wind from 212°, U_n/U_{ref} drops to approximately half the reference wind speed due to the western fjord's sheltering effect. The AoA begins with a negative value at Nautneset, increasing toward Julbo, where it reaches 2°.

4. Conclusions

The present study highlights the critical role of terrain-induced modifications in determining wind characteristics at the Julsundet Bridge site. Through terrain model wind tunnel tests, wind parameters such as mean wind speed, turbulence intensity, pitch and yaw angles, and longitudinal length scales were quantified under various wind directions and their variation along the bridge quantified. To ensure reliable results, inlet conditions in the wind

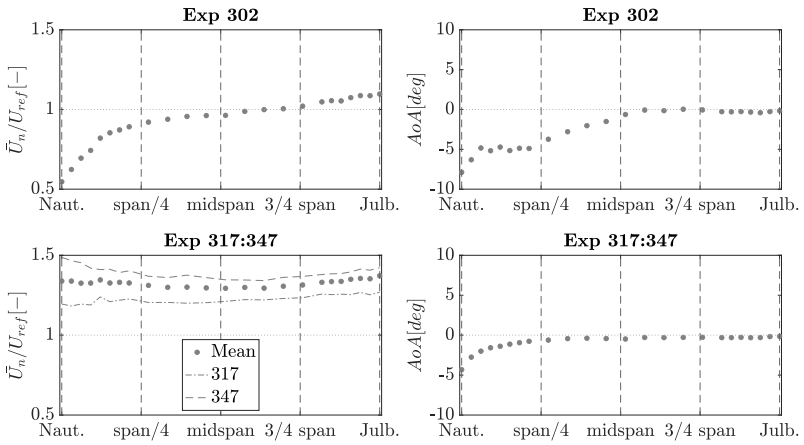

Fig. 14 For the inlet directions from the North, left: normal component of the velocity vector's horizontal plane projection relative to the bridge axis; right: angle of attack.

tunnel were chosen to match the roughness length estimated from full-scale data taken at the bridge site. However, a mismatch between the achieved and target integral length scales was observed. Therefore, results have been presented normalized with respect to the inlet conditions to isolate the impact of terrain on the wind characteristics.

Main findings are summarized as follows:

- Spatial Variability in Wind Characteristics: Significant spatial variations in wind speed and turbulence intensity were observed along the bridge span. Westerly winds exhibited pronounced gradients, with localized reductions in mean wind speed due to sheltering effects and consequent increase of the turbulence intensities. Conversely, southerly and northerly winds resulted in relatively uniform profiles with enhanced channeling effects. These variations confirm the necessity of site-specific wind studies to capture localized phenomena that cannot be identified from a single point measurements.
- Impact of Terrain on Wind Angles: The pitch and yaw angles varied significantly along the bridge axis, reflecting the complex interactions between the flow and surrounding fjord topography. For westerly winds, pronounced downwash effects were observed, whereas easterly and southerly winds exhibited ascent over the fjord near Nautneset.
- Longitudinal Turbulence Scales: The longitudinal turbulence scales demonstrated reductions compared to inlet values for winds aligned with the bridge axis, indicating the generation of smaller turbulent structures due to fjord interactions. For nearly orthogonal wind directions, the scales showed greater consistency with inlet conditions, underscoring the influence of terrain orientation on turbulence properties.
- Coherence of Turbulent Fluctuations: The coherence function analysis revealed variations in spatial correlation along the bridge axis, particularly for wind directions interacting with the steep fjord terrain.

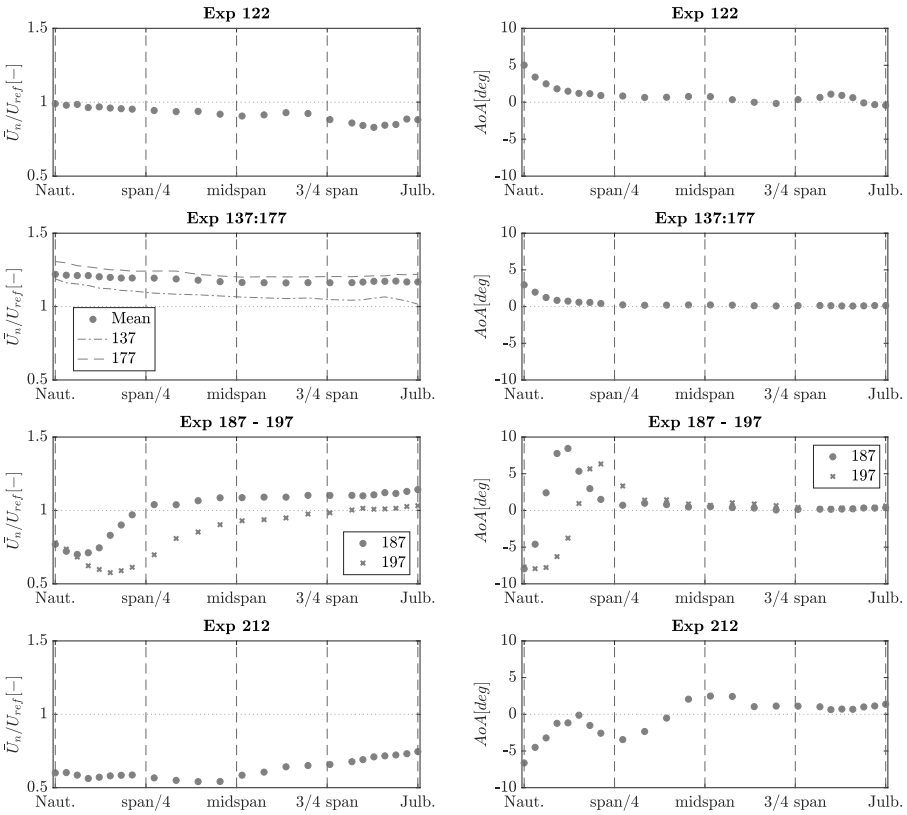

Fig. 15 For the inlet directions from the South, left: normal component of the velocity vector's horizontal plane projection relative to the bridge axis; right: angle of attack.

The results provide a robust dataset to support future studies on the aerodynamic stability of the bridge. By incorporating spatial variations in wind properties along the deck, a more realistic approach can be achieved, moving beyond the traditional assumption of constant wind properties.

Looking ahead, the results from this topographic study can be integrated with the available long-term field measurements at towers' locations. This integration would allow for the extension of localized measurements to characterize wind conditions across the entire bridge span, further improving the reliability of aerodynamic design.

References

Burlando, M., De Gaetano, P., Pizzo, M., Repetto, M. P., Solari, G., and Tizzi, M. (2013), "Wind climate analysis in complex terrains" in Journal of Wind Engineering and Industrial Aerodynamics, 123, 349-362.
https://doi.org/10.1016/j.jweia.2013.09.009

Calamelli, F., Rossi R., Argentini, A., Rocchi, D., and Diana, G. (2024), "A nonlinear approach for the simulation of the buffeting response of long span bridges under non-synoptic storm winds" in Journal of Wind Engineering and Industrial Aerodynamics, 247, 105681.
https://doi.org/10.1016/j.jweia.2024.105681

Castellon, D. F., Fenerci, A., and Øiseth, O. (2022), "Environmental contours for wind-resistant bridge design in complex terrain" in Journal of Wind Engineering and Industrial Aerodynamics, 224, 104943.
https://doi.org/10.1016/j.jweia.2022.104943

Cheynet, E., Jakobsen, J. B., and Snæbjörnsson, J. (2016), "Buffeting response of a suspension bridge in complex terrain" in Engineering Structures, 147, 269-284.
https://doi.org/10.1016/j.engstruct.2016.09.060

Davenport, A. G. (1961), "The spectrum of horizontal gustiness near the ground in high winds" in Quarterly Journal of the Royal Meteorological Society, 87(372), 194–211.
https://doi.org/10.1002/qj.49708737208

Davenport, A. G. (1962), "Buffetting of a suspension bridge by storm winds" in Journal of the Structural Division, 88(3), 233-270.

Davenport, A. G., and King, J. P. C. (1990), "The influence of topography on the dynamic wind loading of long span bridges" in Journal of Wind Engineering and Industrial Aerodynamics, 36, 1373-1382.
https://doi.org/10.1016/0167-6105(90)90133-W

Diana, G., Stoyanoff, S., Aas-Jakobsen, K., Allsop, A., Andersen, M., Argentini, T., Cid Montoya, M., Hernàndez, S., Jurado, J. Á., Katsuchi, H., Kavrakov, I., Kim, H. K., Larose, G., Larsen, A., Morgenthal, G., Øiseth, O., Omarini, S., Rocchi, D., Svendsen, M., and Wu, T. (2020), "IABSE Task Group 3.1 Benchmark Results. Part 1: Numerical Analysis of a Two-Degree-of-Freedom Bridge Deck Section Based on Analytical Aerodynamics" in Structural Engineering International, 30(3), 401-410.
https://doi.org/10.1080/10168664.2019.1639480

Diana, G., Stoyanoff, S., Aas-Jakobsen, K., Allsop, A., Andersen, M., Argentini, T., Cid Montoya, M., Hernàndez, S., Jurado, J. Á., Katsuchi, H., Kavrakov, I., Kim, H. K., Larose, G., Larsen, A., Morgenthal, G., Øiseth, O., Omarini, S., Rocchi, D., Svendsen, M., and Wu, T. (2020), "IABSE Task Group 3.1 Benchmark Results. Part 2: Numerical Analysis of a Three-Degree-of-Freedom

Bridge Deck Section Based on Experimental Aerodynamics" in Structural Engineering International, 30(3), 411-420.
https://doi.org/10.1080/10168664.2019.1661331

Diana, G., Stoyanoff, S., Allsop, A., Amerio, L., Andersen, M. S., Argentini, T., Calamelli, F., Cid Montoya, M., de Ville de Goyet, V., Hernàndez, S., Jurado, J. Á., Kavrakov, I., Larose, G., Larsen, A., Morgenthal, G., Rocchi, D., Svendsen, M. N., and Wu, T. (2022), "IABSE Task Group 3.1 Benchmark Results. Numerical Full Bridge Stability and Buffeting Simulations" in Structural Engineering International, 33(4), 623-634.
https://doi.org/10.1080/10168664.2022.2104188

Fenerci, A., and Øiseth, O. (2017), "Measured buffeting response of a long-span suspension bridge compared with numerical predictions based on design wind spectra" in Journal of Structural Engineering, 143(9), 04017131.
https://doi.org/10.1061/(ASCE)ST.1943-541X.0001812

Fenerci, A., Øiseth, O., and Rønnquist, A. (2017), "Long-term monitoring of wind field characteristics and dynamic response of a long-span suspension bridge in complex terrain" in Engineering Structures, 147, 269-284.
https://doi.org/10.1016/j.engstruct.2017.06.065

Fenerci, A., Lystad, T. M., and Øiseth, O. (2023), "Full-scale monitored wind and response characteristics of a suspension bridge compared with wind tunnel investigations at the design stage" in Journal of Wind Engineering and Industrial Aerodynamics, 242, 105583.
https://doi.org/10.1016/j.jweia.2023.105583

Lystad, T. M., Fenerci, A., and Øiseth, O. (2018), "Evaluation of mast measurements and wind tunnel terrain models to describe spatially variable wind field characteristics for long-span bridge design" in Journal of Wind Engineering and Industrial Aerodynamics, 179, 558-573.
https://doi.org/10.1016/j.jweia.2018.06.021

Midjiyawa, Z., Cheynet, E., Reuder, J., Ágústsson, H., and Kvamsdal, T. (2021), "Potential and challenges of wind measurements using met-masts in complex topography for bridge design: Part I – Integral flow characteristics" in Journal of Wind Engineering and Industrial Aerodynamics, 211, 104584.
https://doi.org/10.1016/j.jweia.2021.104584

Midjiyawa, Z., Cheynet, E., Reuder, J., Ágústsson, H., and Kvamsdal, T. (2021), "Potential and challenges of wind measurements using met-masts in complex topography for bridge design: Part II – Spectral flow characteristics" in Journal of Wind Engineering and Industrial Aerodynamics, 211, 104585.
https://doi.org/10.1016/j.jweia.2021.104585

Peng, Y., Wang, S., and Li, J. (2018), "Field measurement and investigation of spatial coherence for near-surface strong winds in Southeast China" in Journal of Wind Engineering and Industrial Aerodynamics, 172, 423-440.
https://doi.org/10.1016/j.jweia.2018.01.013

Ropelewski, C. F., Tennekes, H., and Panofsky, H. A. (1973), "Horizontal coherence of wind fluctuations" in Boundary-Layer Meteorology, 5, 353–363.
https://doi.org/10.1007/BF00155243

Scanlan, R. H. (1978), "The action of flexible bridges under wind, II: Buffeting theory" in Journal of Sound and Vibration, 60(2), 201-211.
https://doi.org/10.1016/0022-460X(78)90354-7

Solari, G., and Piccardo, G. (2001), "Probabilistic 3-D turbulence modeling for gust buffeting of

structures" in Probabilistic Engineering Mechanics, 16(1), 73-86.
https://doi.org/10.1016/S0266-8920(00)00010-2

Turbulent Flow Instrumentation, Cobra Probe Flyer. Available online: https://www.turbulentflow.com.au/Downloads/Flyer_CobraProbe.pdf (accessed on 3 July 2025).

Yu, J., Chen, X., Li, M., Li, M., and Li, M. (2024), "Application of numerical methods in the estimation of design wind velocity for bridges in mountainous areas" in Journal of Wind Engineering and Industrial Aerodynamics, 250, 105764.
https://doi.org/10.1016/j.jweia.2023.105764

Zhang, M., Jiang, F., Zhang, J., Qin, J., Jiang, X., and Li, Y. (2022), "Field measurement of local wind environment on the approach deck of a suspension bridge in mountain terrain" in Scientific Reports, 12(1), 15659.
https://doi.org/10.1038/s41598-022-19597-6